An improved limited area model for describing the dust cycle in the atmosphere

C. Spyrou,[1] C. Mitsakou,[1] G. Kallos,[1] P. Louka,[1] and G. Vlastou[1]

Received 8 December 2009; revised 1 April 2010; accepted 12 April 2010; published 15 September 2010.

[1] During the last decade, several numerical schemes have been deployed for the simulation of mineral dust processes in the atmosphere. The developed models have various deficiencies in the representation of dust particle physical properties and effects on climate. On the basis of the present status of the dust modeling tools, a combined effort was devoted to upgrading the SKIRON/Dust forecasting system by incorporating new features for the description of the lower boundary characteristics of the atmospheric model and the dust aerosol properties. In this paper, the updated model version is presented along with sensitivity simulations and evaluation of the model results with available observational data. The analysis is separated into two main parts, namely, the improvements that correspond to the atmospheric modeling system SKIRON and the upgrading of the physical mechanisms incorporated in the dust transport submodel. The analysis showed that the incorporation of the new model correction schemes led to a better and more accurate representation of the processes concerning meteorology and dust properties. The new soil characterization schemes significantly improve the energy-partitioning predictions at the surface and therefore the boundary layer processes that play a substantial role in the determination of the dust production mechanisms. Significant differences were detected in the radiation balance between atmosphere and ground surface by incorporating statistical corrections for the description of terrain slopes and azimuths, mainly in areas with highly rough terrain. Finally, the more accurate description of the transported dust aerosol distribution (eight size bins) and the new dust production and deposition schemes led to more efficient determination of the dust particle optical properties (aerosol optical depths).

Citation: Spyrou, C., C. Mitsakou, G. Kallos, P. Louka, and G. Vlastou (2010), An improved limited area model for describing the dust cycle in the atmosphere, *J. Geophys. Res.*, *115*, D17211, doi:10.1029/2009JD013682.

1. Introduction

[2] Large amounts of mineral dust are produced by wind erosion in arid and semi-arid areas and under favorable weather conditions can travel over long distances affecting the environment of remote areas in many ways. In principal, dust particles modify the planetary albedo affect and reduce the amount of radiation reaching the Earth's surface by scattering and absorbing solar radiation [*Yu et al.*, 2001]. Natural and anthropogenic aerosols act as cloud condensation nuclei or ice nuclei, thus modifying the microphysical, microchemical, and, hence, optical and radiative properties of clouds [*Charlson et al.*, 1991]. Also, combined with certain anthropogenic pollutants, they can contribute to the occurrence of heavy precipitation events [*Levin et al.*, 2005; *Kelly et al.*, 2007].

[3] The simulation of the mineral dust cycle is an intriguing task and requires extending study since the physical processes (production, transport, and deposition) that determine the fate of dust particles are rather complicated. Since the late 1990s, various research groups and government agencies, especially in countries affected by dust transport, have attempted to develop advanced modeling techniques targeting better simulations of dust production, transport, transformation, and deposition patterns as complementary tools to observations. In addition, it has been realized that there is a need for a better understanding of the aerosol cycle in the atmosphere and its potential impacts and interactions with climate.

[4] The first numerical attempts on the simulation of mineral dust processes in the atmosphere have been based on both global- and regional-scale atmospheric models. The global-scale models, such as Goddard Chemistry Aerosol Radiation and Transport [*Ginoux et al.*, 2001] and Dust Entrainment and Deposition (DEAD) [*Zender et al.*, 2003], have typical horizontal resolution of 2.5° or 1° at best. However, mineral dust transport also leads to more regional atmospheric impacts, such as air quality degradation and radiative effects on climate. Thus, the development of limited area atmospheric models that simulate the mineral dust

[1]School of Physics, University of Athens, Athens, Greece.

0148-0227/10/2009JD013682

cycle is essential. Among the first steps toward the study of dust processes by utilizing regional-scale models is including the case of the dust microphysical aerosol model [*Liu et al.*, 2003] that was embedded in the COAMPS atmospheric model [*Hodur*, 1997] and the case of the SKIRON/Dust system [*Nickovic et al.*, 2001; *Papadopoulos*, 2001] with online coupling of the dust cycle mechanisms on the SKIRON version of the eta atmospheric model [*Kallos et al.*, 1997]. The chemical transport model Chemical Weather Forecast System driven by the Regional Atmospheric Modeling System has also been used for the simulation of dust aerosol transport [*Uno et al.*, 2003], where the authors outlined the need to improve the description of dust emissions in the model. The Regional Climate Model coupled with a desert dust module has been implemented for the study of dust episodes during African dust outbreaks [*Zakey et al.*, 2006]. In this study, the model physical algorithms were proved rather insufficient for the capture of specific dust transport patterns, as the authors claim. The modeling efforts of *Gong et al.* [2003] and *Song and Carmichael* [2001] are other examples of the incorporation of dust processes in regional-scale models. A regional dust model system, LM-MUSCAT-DES, also has been developed during the 2006 Saharan Mineral Dust Experiment field campaign [*Heinold et al.*, 2008], with a subsequent model evaluation revealing the benefits and the limitations of the model, such as inaccuracies in the location of dust sources and the description of specific meteorological features by the model. Recently, the Met Office Unified Model has been upgraded so as to include the dust emissions scheme based on the DEAD model [*Ackerley et al.*, 2009]. The necessity for sand and dust storm prediction in East Asia has led to the development of CUACE/Dust operational forecasting system [*Zhou et al.*, 2008]; the model evaluation revealed the significance of the utilization of detailed soil description. The intercomparison study performed over Asia by *Uno et al.* [2006] with the implementation of various dust models produced quite different results while estimating dust concentration and fluxes. The wide scattering of the calculated values was found to be generated by the different dust emission/deposition schemes and dust particle size representation, as well as the surface boundary data, such as the soil texture and the land use data. Thus, the simulation efficiency of the modeling systems is expected to be improved by the incorporation of the most recently updated and accurate descriptions of the above mentioned parameters.

[5] A combined effort has been devoted by the Atmospheric Modeling and Weather Forecasting Group (AM&WFG) of the University of Athens for the development and continuous upgrading of the SKIRON/Dust forecasting system [*Kallos et al.*, 1997; *Nickovic et al.*, 2001] in response to the need to simulate the mineral dust cycle as accurately as possible by incorporating new features for the description of the lower boundary (ground or sea surface) characteristics of the atmospheric model and the dust aerosol properties. In this study, the newest model version is discussed in detail along with sensitivity runs and evaluation of the model components with the aid of available observational data. The analysis is divided in two main parts describing separately the improvements that correspond to the two numerical codes that are coupled: (1) the atmospheric modeling system SKIRON and (2) the dust transport submodel. More specifically, the new schemes incorporated in the atmospheric modeling system are mainly related to the description of the soil characteristics (updated soil texture characterization and land use (vegetation) maps). Moreover, the surface variability expressed by tilted surfaces and orientation has been introduced in both surface energy partitioning and dust productivity. The improvements in the dust transport submodel include the incorporation of eight size bins of dust particles [*Zender et al.*, 2003; *Pérez et al.*, 2006], the calculation of aerosol optical depth (AOD), and the correction of radiative transfer due to the presence of dust particles. Also, the replacement of the dry and wet deposition schemes with more accurate ones and the in-cloud scavenging have been applied. The new version of SKIRON modeling system has been used recently in operational forecasting over a large area from the Caspian Sea to the western United States and from the tropics to the Arctic region. The model is easily configurable for any place globally. For the present runs, we selected the area covering the wider Mediterranean region, so as to test the simulation efficiency in response to the atmospheric and dust related parameters in dust affected areas (e.g., southern Europe).

[6] The next section describes the modeling system SKIRON/Dust at its older form and section 3 outlines the new schemes that have been incorporated in the modeling system. The sensitivity model runs and the evaluation processes are presented in section 4. Finally, the concluding remarks of the model upgrading are summarized in section 5.

2. SKIRON/Dust Modeling System

[7] SKIRON is a modeling system developed at the University of Athens from the AM&WFG [*Kallos et al.*, 1997, 2006] in the framework of the nationally and European Union (EU)-funded projects SKIRON, Mediterranean Dust Experiment (MEDUSE), Atmospheric Deposition and Impact on the Open Mediterranean Sea (ADIOS), and recently Climate Change and Impact Research (CIRCE). Many groups use the model for research and operational purposes. In some areas, it is used with the name DREAM that comes from the dust submodel as it has been developed at the University of Athens [*Nickovic et al.*, 2001]. The atmospheric model is based on the ETA/National Centers for Environmental Prediction (NCEP) model, which was originally developed by *Mesinger* [1984] and *Janjic* [1984] at the University of Belgrade. Details on the various model parameterization schemes (i.e., Monin-Obukhov similarity model, Betts-Miller-Janjic convection scheme) can be found in the above mentioned studies and references therein. During the preprocessing phase of the atmospheric model, it is identified whether a grid point will act as a desert dust source according to its corresponding soil and land cover. The production rates are specified according to land cover, soil characteristics, and specific conditions (e.g., moisture content, composition, and mineralogy). The predicted atmospheric and hydrological conditions are used in order to calculate the effective rates of the injected dust concentration based on the viscous/turbulent mixing, shear-free convection, diffusion, and soil moisture. The dust module [*Nickovic et al.*, 2001; *Papadopoulos*, 2001] in-

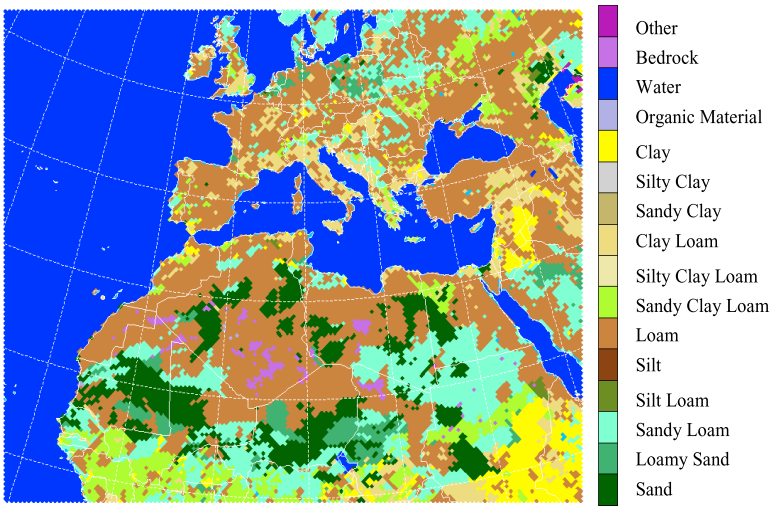

Figure 1. Soil texture database: 16 category hybrid STATSGO/FAO 30″.

cludes the effects of the particle size distribution in order to simulate size-dependent processes more accurately. Recent improvements and modifications of the transport part of the model have been made in order to make this module available as a separate plug-in to the entire system, which can be easily switched on/off according to the needs and applications.

3. New Model Features

3.1. Soil Characteristics and Dust Production

[8] Surface properties, such as soil moisture, heat storage, and conductivity, together with canopy, determine the partitioning of the incoming solar radiation that gets absorbed by the ground into sensible, latent, and ground heat fluxes as well as the surface albedo. These processes in turn strongly influence the air temperature and humidity close to the ground level, the turbulence, and in general the atmospheric boundary layer structure [*Segal et al.*, 1989]. The differential gradient of the various surface parameters generates thermal circulations (i.e., terrain-induced mesoscale systems), such as sea or land breezes, mountain valley winds, and urban circulations. Moreover, the soil characteristics, and in particular the land use characterization (e.g., barren or sparsely vegetated), determine the production efficiency of dust aerosols by mechanical processes and their physical properties (concentration, size distribution). Therefore, the incorporation of the finest and more detailed data sets for the description of the surface boundary of the modeling system is rather crucial.

[9] The lower boundary of the modeling system is determined by two primary variables, namely, the soil texture and the vegetation type, which specify other secondary parameters, such as the minimal canopy resistance and soil hydraulic properties. Moreover, the ground surface consists of topographic inhomogeneities, such as small hills and valleys of different slope and orientation. These variations of the topography and especially the orientation and inclination of the terrain with respect to the Sun is a critical parameter for the evaluation of the amount of solar radiation reaching the soil surface. Thus, an additional effort has been made for the correction of the incoming solar radiation by considering terrain slopes.

[10] The sea surface temperature (SST) determines the air-sea interaction and consequently the land-sea temperature contrast in specific coastal areas. Thus, it is essential to apply highly resolved and daily updated SST fields in the modeling system.

[11] The various model improvements related to the ground characteristics are described in detail in the following paragraphs.

3.1.1. New Soil and Vegetation Characterization

[12] In the old model version [*Nickovic et al.*, 2001; *Papadopoulos*, 2001], the soil characterization is based on the 1° × 1° ZÖBLER/FAO soil map [Zöbler, 1986] and the 14 category *SiB vegetation* data set [Dorman *and Sellers*, 1989] is used. In the upgraded model version, the 30 s soil texture database developed by *Miller and White* [1998] based on the U.S. Department of Agriculture's State Soil Geographic Database (Figure 1) has replaced the older one. It was derived by using the 1 km resolution multilayer 16 category soil characteristics data set and provides information on the soil texture, bulk density, porosity, available water capacity, and other soil physical properties. The model has the option for defining the number of patches considered at each grid cell. In the present configuration, the two dominant soil categories are considered for each model grid cell based on the highly resolved soil database and the surface parameters of both of them are taken into consideration with the respective percentage. The present data set provides also the capability of expanding it to include three additional categories, namely, "Playa," "Lava," and "White sand." This could be highly beneficial for studies on unique land cover types found in some limited areas. In the SKIRON modeling system, we used the soil texture class of the first surface soil layer of the data set. The different soil parameters that are required by the atmospheric modeling system—soil porosity, saturated moisture potential, satu-

Table 1. Thermophysical Parameters for the Different Soil Textures[a]

b Parameter	Air Dry Soil Moisture Content Limits	Maximum Soil Moisture Content Porosity (m^3 m^{-3})	Saturated Soil Potential (m)	Saturated Soil Hydraulic Conductivity (m s^{-1})	Soil Texture
2.79	0.01	0.339	0.069	1.07E-06	Sand
4.26	0.028	0.421	0.036	1.41E-05	Loamy sand
4.74	0.047	0.434	0.141	5.23E-06	Sandy loam
5.33	0.084	0.476	0.759	2.81E-06	Silt loam
5.33	0.084	0.476	0.759	2.81E-06	Silt
5.25	0.066	0.439	0.355	3.38E-06	Loam
6.66	0.067	0.404	0.135	4.45E-06	Sandy clay loam
8.72	0.12	0.464	0.617	2.04E-06	Silty clay loam
8.17	0.103	0.465	0.263	2.45E-06	Clay loam
10.73	0.1	0.406	0.098	7.22E-06	Sandy clay
10.39	0.126	0.468	0.324	1.34E-06	Silty clay
11.55	0.138	0.468	0.468	9.74E-07	Clay
5.25	0.066	0.439	0.355	3.38E-06	Organic material
0	0	1	0	0	Water
2.79	0.006	0.2	0.069	1.41E-04	Bedrock
4.26	0.028	0.421	0.036	1.41E-05	Other (land-ice)

[a]Data from http://www.rap.ucar.edu.

rated hydraulic conductivity, and wilting moisture content—are provided by the database (see Table 1).

[13] A 30 s global land use/cover database has been utilized, which is classified according to the 24 category U.S. Geological Survey (USGS) land use/cover system [*Anderson et al.*, 1976] (Table 2). This global database was obtained from the 1 km advanced very high resolution radiometer data set that spans the period from April 1992 through March 1993. Urban areas have been also added to the data set with the contribution of the Development of the Digital Chart of the World (Defense Mapping Agency, 1992). The latter data was based on photogrammetric analyses of the U.S. Department of Defense Corona imagery acquired in the 1960s [*Grossman-Clarke et al.*, 2005]. This high-resolution land use data set provides a detailed spatial distribution of vegetation as well as delineation between water bodies and land surface for SKIRON high-resolution applications. The dominant vegetation type in each grid box is selected to represent the "grid level" vegetation characteristics. The new vegetation map as utilized by the SKIRON modeling system for various test runs for the purpose of this paper is depicted in Figure 2.

3.1.2. Incoming Solar Radiation Over Slant Surfaces

[14] The orientation of the slopes with respect to the position of the Sun determines the incoming solar radiation that reaches the ground surface. Since the topographic variability (slant surface orientation) cannot be accurately represented in the model grids, a new processor has been developed that derives statistics for the slope steepness and

Table 2. Physical Characteristics for the Different Vegetation Types[a]

Surface Albedo	Rougness Length (m)	Minimum Stomatal Resistance (s m^{-1})	R_{gl} Parameter (Radiation Stress Function)	*hs* Parameter (Vapor Pressure Deficit Function)	Vegetation Type
0.15	1	200	999	999	Urban and built-up land
0.19	0.07	40	100	36.25	Dryland cropland and pasture
0.15	0.07	40	100	36.25	Irrigated cropland and pasture
0.17	0.07	40	100	36.25	Mixed dryland/irrigated cropland and pasture
0.19	0.07	40	100	36.25	Cropland/grassland mosaic
0.19	0.15	70	65	44.14	Cropland/woodland mosaic
0.19	0.08	40	100	36.35	Grassland
0.25	0.03	300	100	42	Shrubland
0.23	0.05	170	100	39.18	Mixed shrubland/grassland
0.2	0.86	70	65	54.53	Savanna
0.12	0.8	100	30	54.53	Deciduous broadleaf forest
0.11	0.85	150	30	47.35	Deciduous needleleaf forest
0.11	2.65	150	30	41.69	Evergreen broadleaf forest
0.1	1.09	125	30	47.35	Evergreen needleleaf forest
0.12	0.8	125	30	51.93	Mixed forest
0.19	0.001	100	30	51.75	Water bodies
0.12	0.04	40	100	60	Herbaceous wetland
0.12	0.05	100	30	51.93	Wooded wetland
0.12	0.01	999	999	999	Barren or sparsely vegetated
0.16	0.04	150	100	42	Herbaceous tundra
0.16	0.06	150	100	42	Wooded tundra
0.16	0.05	150	100	42	Mixed tundra
0.17	0.03	200	100	42	Bare ground tundra
0.7	0.001	999	999	999	Snow or ice

[a]Data from http://www.rap.ucar.edu.

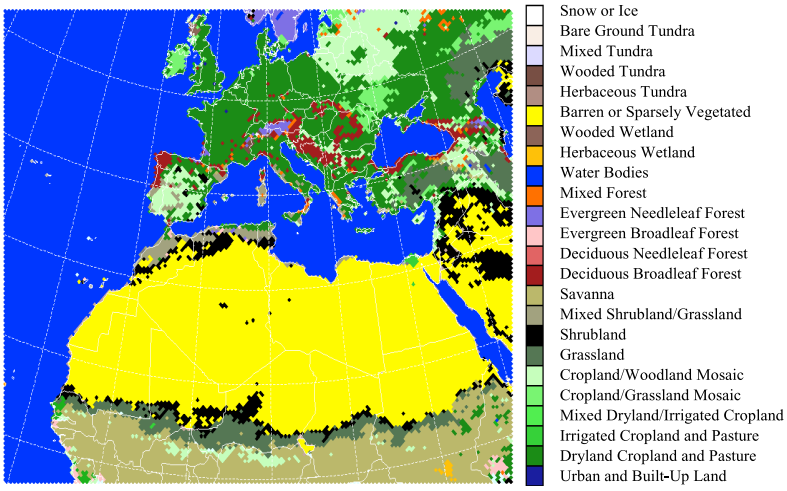

Figure 2. Vegetation map: 24 category U.S. Geological Survey 30″.

orientation. A major advantage of the more accurate representation of terrain sloping in the atmospheric model is the efficiency of better positioning of the convergence zones at the mountainous regions.

[15] The derived statistics are used to correct the shortwave (SW) radiation reaching the ground for each grid box of the model. According to *Pielke* [2002], the amount of the direct solar radiation that reaches a sloping terrain F_d^{sl} is determined as a fraction of the solar radiation that would reach a flat surface F_d^f by equation (1):

$$F_d^{sl} = F_d^f \cdot \frac{\cos i}{\cos Z} \tag{1}$$

where cos$i$ is the cosine of the angle at which direct solar radiation impinges on sloping terrain and can be determined by the following equation:

$$\cos i = \cos\alpha \cdot \cos Z + \sin\alpha \cdot \sin Z \cdot \cos(\beta - \gamma) \tag{2}$$

The parameter α is the slope of the terrain $\left(\alpha = \tan^{-1}\left[\left(\left(\frac{\partial z_g}{\partial x}\right)^2 + \left(\frac{\partial z_g}{\partial y}\right)^2\right)^{1/2}\right]\right)$, where z_g is the terrain height. The azimuths β and γ refer to the Sun $\left(\beta = \sin^{-1}\left(\frac{\cos(DEC)\cdot\sin(HRLCL)}{\sin Z}\right)\right)$ and the slope of terrain $\left(\gamma = \pi/2 - \tan^{-1}\left[\left(\frac{\partial z_g}{\partial x}\right)/\left(\frac{\partial z_g}{\partial y}\right)\right]\right)$, respectively. The zenith angle Z is calculated at each grid point and at each computational time step by equation (3):

$$\cos Z = \sin(DEC)\cdot\sin\varphi + \cos(DEC)\cdot\cos(HRLCL)\cdot\cos\varphi \tag{3}$$

where DEC is the declination of the Sun that ranges between +23.44° (on 21 June) and –23.44° (on 22 December), φ is the geographical latitude of each grid point, and $HRLCL$ is the hour angle.

[16] Equations (1)–(3) are implemented separately on each grid box of the original high-resolution (30″) topographic data set. Then, for each ETA grid box a mean slope α_{mean} and the respective azimuth γ are determined, as proposed by *Steyn* [1976]. In particular, the azimuth γ is defined as a function of the four main orientations only (west, south, east, and north) for mathematical simplicity. Then, the frequency of occurrence f of the azimuth at each one of the directions is determined. Consequently, following the above approximations, the angle i between the direct solar radiation and the sloping terrain can be calculated by equation (4):

$$\begin{aligned}\cos i = {} & f_{north}\cdot(\cos\alpha_{mean}\cdot\cos Z + \sin\alpha_{mean}\cdot\sin Z\cdot\cos(\beta-\pi)) \\ & + f_{east}\cdot(\cos\alpha_{mean}\cdot\cos Z + \sin\alpha_{mean}\cdot\sin Z\cdot\cos(\beta-\pi/2)) \\ & + f_{south}\cdot(\cos\alpha_{mean}\cdot\cos Z + \sin\alpha_{mean}\cdot\sin Z\cdot\cos(\beta-0)) \\ & + f_{west}\cdot(\cos\alpha_{mean}\cdot\cos Z + \sin\alpha_{mean}\cdot\sin Z\cdot\cos(\beta-3\cdot\pi/2)) \\ & + f_{flat}\cdot(\cos\alpha_{mean}\cdot\cos Z)\end{aligned} \tag{4}$$

In Figure 3, the dominant orientation and the slope inclination of the ETA grid boxes are shown, respectively, for the model configuration selected in the present study. High variability of the terrain orientation can be observed, while the occurrence of perfectly flat areas is considered sparse throughout the model domain. However, the terrain inclination is quasi-flat (lower that 5°) in the greatest part (about 90%) of the domain surface. The implementation of the corrections proposed in the present section is more essential in cases of high horizontal grid resolution (grid increment ≤1/4°) and in areas of steep slopes and rapidly varying topography. The present corrections are also important in cases of coarse model grid resolution, since the topographic variability, which would be otherwise neglected, is taken into consideration by incorporating the above statistics. The consideration of the slopes and azimuths of the terrain provides a better surface energy partitioning at the ground and therefore affects the determination of boundary layer structure and dust production.

3.1.3. Sea Surface Temperature

[17] The system has the capability to use SST fields from various sources and with different resolutions. It can be used either as constant during the simulation or variable nudging the fields during the run. Alternatively, the system can uti-

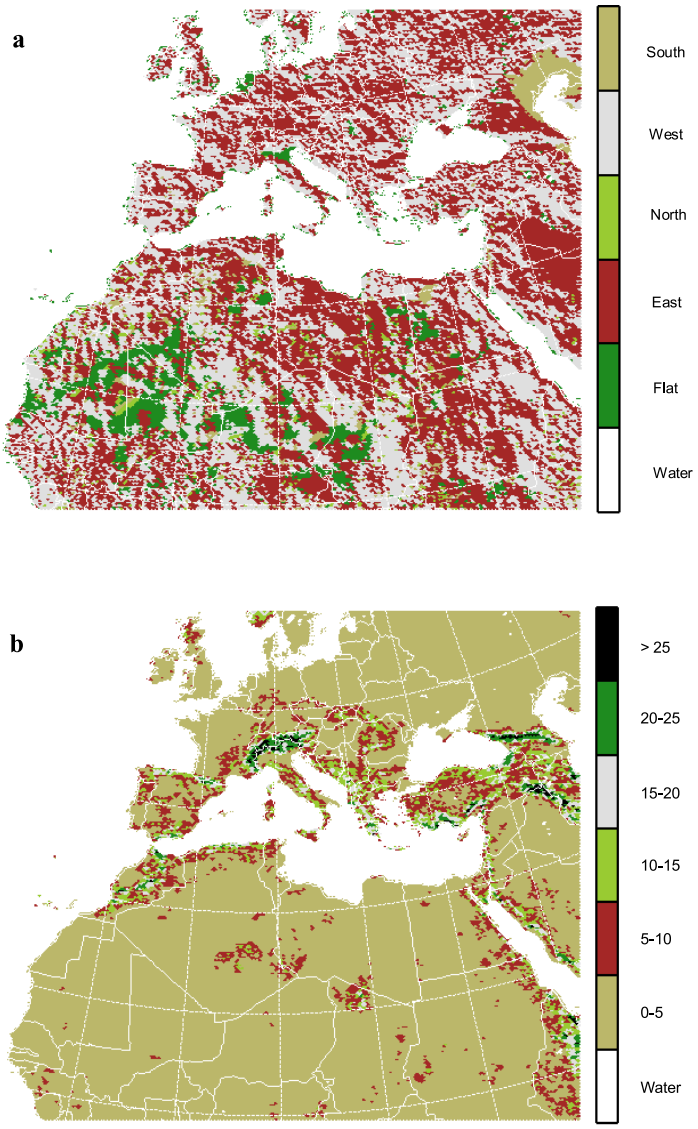

Figure 3. (a) Dominant orientation and (b) slope inclination in degrees in each grid box.

lize predicted SST values from 3-D hydrodynamic models, as selected in the present study. In particular, the system utilized the SST fields from the NCEP with a resolution of 0.5°. It should be noted that during model simulations, in case that the initial and boundary meteorological conditions are provided by the European Center for Medium Range Weather Forecast (ECMWF) analyses, the SST fields are also taken from ECMWF. In specific case studies performed with the SKIRON model, more highly resolved SST fields have also been used, following the study of the atmospheric response over Europe and Mediterranean regions to tropical Pacific SST perturbations prepared by *Katsafados et al.* [2005].

3.2. Description of Dust Submodel

3.2.1. Size Distribution: Bin Method

[18] The older model version [*Nickovic et al.*, 2001; *Papadopoulos*, 2001] uses four bins for the description of dust particle size distribution (centered diameters of 1.5, 12, 36, and 76 μm) throughout the whole model domain. In the new version of SKIRON, a modal representation of the particle size is used for a more accurate description of the aerosol mass distribution over the source areas, as well as for the description of long-range transported dust particles. Over the source areas, the mass distribution is described by the three-modal lognormal function of *D'Almeida* [1987], as described in detail by *Zender et al.* [2003]. Although dust production is initiated by the entrainment of sand-sized particles (~60 μm in diameter), only smaller particles with radius $r \leq 10$ μm reside in the atmosphere long enough to be transported over large distances. Thus, for the long-range traveling particles, the transport mode proposed by *Schulz et al.* [1998] and tested by *Zender et al.* [2003] has been applied. More specifically, the dust particle size distribution follows a lognormal form with mass median diameter equal to 2.524 μm and geometric standard deviation equal to $\sigma = 2$. Currently, the transport mode uses eight size bins with effective radii of 0.15, 0.25, 0.45, 0.78, 1.3, 2.2, 3.8, and 7.1 μm, similar to the size bins selected

by *Pérez et al.* [2006]. More size bins can be added in case studies related to sand storms and local effects.

3.2.2. Dust Production

[19] In the older model version, the dust aerosol production was initiated by the surface wind, as soil particles drift when the wind velocity exceeds a threshold value. However, the finest particles cannot be directly suspended by the wind because of strong cohesive forces, as already mentioned by *Zender et al.* [2003]. In the new model version, dust particles are assumed to be mobilized through the process of saltation bombardment [*Alfaro and Gomes*, 2001; *Bagnold*, 2005]. Thus, clay and silt-sized particles are produced from sand-sized soil aggregates (>60 μm) when the latter ones impact the soil during their saltation trajectories [*Gillette*, 1977].

[20] For the initiation of the saltation process, the turbulent drag force of the surface wind must overcome the gravitational inertia of the sand particles. The friction velocity u_*, which can be easily computed from standard meteorological fields, is the parameter that determines the saltation efficiency. The mass of particles injected into the atmosphere depends on the excess of the friction velocity over the threshold friction velocity required for saltation. The threshold friction velocity can be parameterized using an empirical formula of the friction Reynolds number ReF [*Marticorena et al.*, 1997]:

$$\mathrm{Re}F = 1331 \cdot D_{opt}^{1.56} + 0.38 \tag{5}$$

Where D_{opt} = ~60 μm is the optimum particle size for which the threshold friction velocity is minimum [*Iversen et al.*, 1976].). On the basis of semi-empirical relationships derived from experiments in wind tunnels, the threshold friction velocity can be expressed as follows:

$$U_*^{thres} = \begin{cases} \dfrac{0.129 \cdot \left(\frac{\rho_p g D_{opt}}{\rho_\alpha}\right)}{\left(1.928\mathrm{Re}F^{0.092} - 1\right)^{0.5}} & 0.03 < \mathrm{Re}F < 10 \\ 0.12 \cdot \left(\dfrac{\rho_p g D_{opt}}{\rho_\alpha}\right)\left(1 - 0.0858 e^{-0.0617(\mathrm{Re}F - 10)}\right) & \mathrm{Re}F > 10 \end{cases} \tag{6}$$

where ρ_p is the particle density, ρ_a is the air density, and g is the gravitational acceleration. By assuming that all soil types in arid and semi-arid areas contain particles with sizes that could provoke saltation bombardment, dust production is initiated when u_* exceeds U_*^{thres} [*Zender et al.*, 2003].

[21] The threshold friction velocity is highly dependent on the ground wetness. The maximum amount of absorbed water W_t can be derived from the empirical formula of *Fécan et al.* [1999] as a function of the soil clay fraction:

$$W_t = 0.014 \cdot (\%\mathrm{Clay})^2 + 0.17 \cdot (\%\mathrm{Clay}) \tag{7}$$

[22] Then, the dependence of the threshold friction velocity on the soil water can be expressed as:

$$U_*^{thres} = \begin{cases} U_*^{thres} & W \le W_t \\ U_*^{thres} \cdot \sqrt{1 + 1.21(W - W_t)^{0.68}} & W > W_t \end{cases} \tag{8}$$

Where W is the soil moisture.

[23] Finally, the scheme proposed by *Marticorena and Bergametti* [1995] was adopted for the calculation of the mass flux. In particular, the horizontally saltating mass flux of large particles derives from the formula of *White* [1979]:

$$HFLX = \frac{C\rho_a u_*^3}{g}\left(1 - \frac{U_*^{thres}}{u_*}\right)\left(1 + \frac{U_*^{thres}}{u_*}\right)^2 \tag{9}$$

Where C = 2.61. The vertical saltating flux $VFLX$ is calculated through the fraction $VFLX/HFLX$ and the soil clay content (%Clay) as following:

$$VFLX/HFLX = e^{0.134(\%\mathrm{Clay}) - 6} \tag{10}$$

[24] Since equation (10) provides adequate results for 0% < (%Clay) < 20% and because of the lack of a more accurate approximation of the relationship between $VFLX$ and $HFLX$ for soil content values greater than the upper limit, its value is then reduced to 20%, so as to allow for the use of equation (10). Note that an analytical clay content database with resolution 0.08° × 0.08° [*Reynolds et al.*, 1999] is utilized, providing a detailed representation of the clay fraction in desert areas and leading to an accurate determination of the saltating mass efficiency.

3.2.3. Dust Deposition

3.2.3.1. Dry Deposition Scheme

[25] With regard to the simulation of particle dry deposition, the deposition velocities corresponding to various physical processes (diffusion, impaction, gravitational settling) that lead to deposition onto surfaces are calculated. The scheme introduced by *Georgi* [1986], which included empirical formulas and parameter values, was used in the older SKIRON version [*Nickovic et al.*, 2001]. Here, it has been substituted by the one resulting from the resistance approach, which is similar to that implemented in UAM-AERO [*Kumar et al.*, 1996]. Thus, particle deposition velocity is calculated using the following resistance equation:

$$V_d = V_{sed} + \frac{1}{r_a + r_b + r_a r_b V_{sed}} \tag{11}$$

where $r_a = \frac{1}{ku_*}\left[\ln\left(\frac{1}{z_0}\right) - \varphi_h\right]$ and $r_b = \frac{1}{u_*\left(S_c^{-2/3} + 10^{-3/S_t}\right)}$ are the aerodynamic and boundary resistances, respectively, k is the von Karman's constant, z_0 is the surface roughness length, φ_h is a stability correction term, S_c is the Schmidt number, S_t is the Stokes number that characterizes the atmospheric air flow, and V_{sed} is the gravitational terminal settling velocity, as defined by the Stokes' law. The new dry deposition scheme is applied separately for each particle size bin and model grid point.

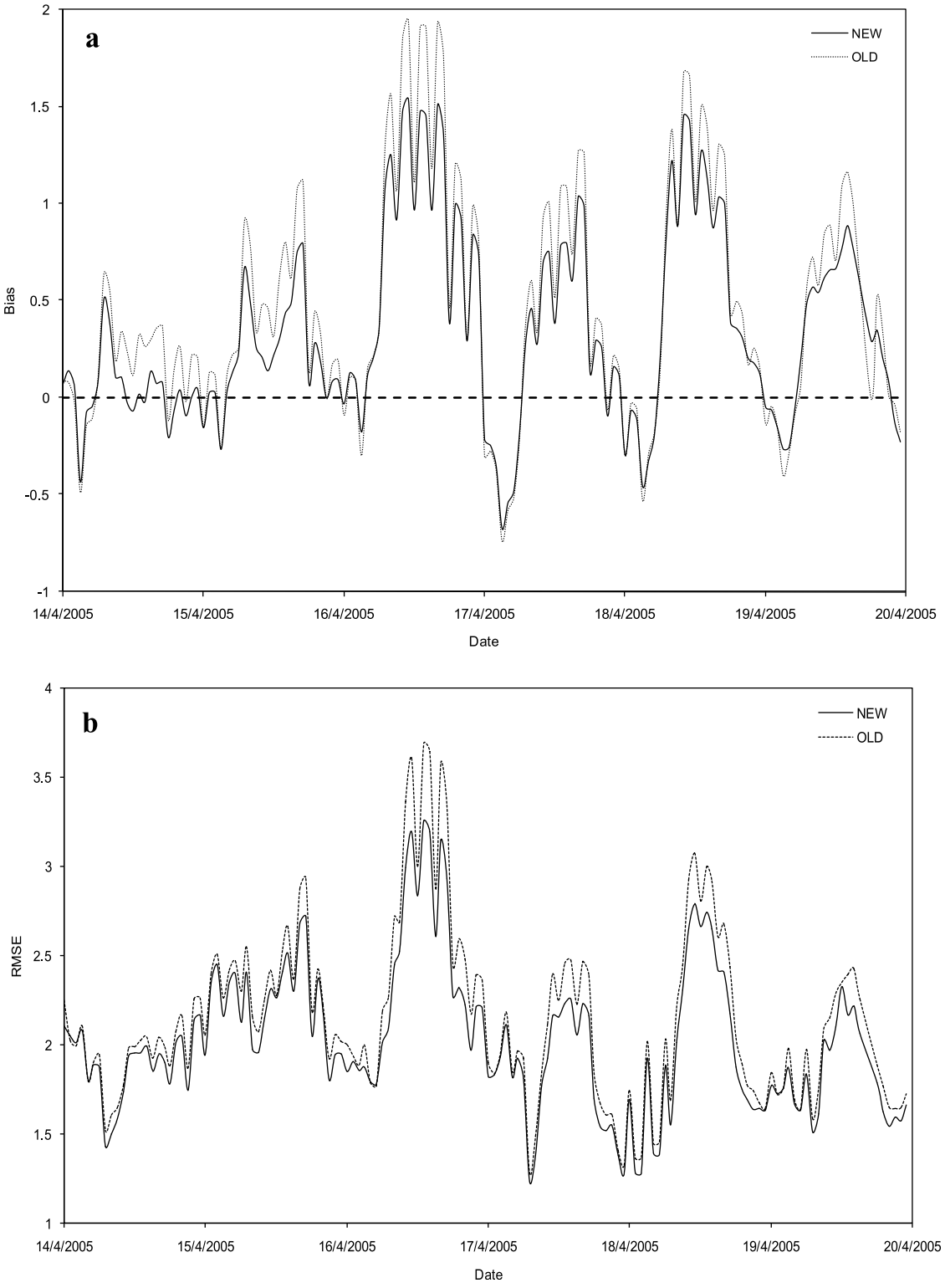

Figure 4. Model (a) bias and (b) RMSE of 2 m temperature starting from 0000 UTC as derived by the NEW and OLD model soil topography.

3.2.3.2. Wet Deposition Scheme

[26] In the updated modeling system, the particle scavenging process includes both in-cloud and below-cloud removal mechanisms. The temporal variation of the particle concentration $\partial C/\partial t$ within or below a precipitating cloud depends on a scavenging coefficient Λ: $\frac{\partial C}{\partial t} = -\Lambda C$. In the old model version [*Nickovic et al.*, 2001], the coefficient Λ was taken to be constant. In the new model version, this has been corrected by using equation (12) that was proposed by

Table 3. Statistical Parameters for 2 m Temperature as Derived by the NEW and OLD Model Soil Topography

Month and Year	Bias	RMSE	Correlation Coefficient
	NEW Soil		
Apr 2005	0.35 ± 0.02	2.14 ± 0.02	0.89
Apr 2006	0.39 ± 0.02	2.14 ± 0.03	0.90
Apr 2007	0.35 ± 0.02	2.13 ± 0.02	0.90
	OLD Soil		
Apr 2005	0.46 ± 0.02	2.23 ± 0.03	0.89
Apr 2006	0.48 ± 0.02	2.24 ± 0.03	0.90
Apr 2007	0.41 ± 0.02	2.18 ± 0.02	0.89

Seinfeld and Pandis [1998] and adopted from the CAMx model [*Environ*, 2006] for aerosols inside clouds:

$$\Lambda_c = 4.2 \times 10^{-7} \frac{EP}{d_d} \tag{12}$$

Where E is the collection efficiency, P is the precipitation rate, and d_d is the cloud drop diameter as calculated by the atmospheric model, for the estimation of the raindrop fall speed at the bottom of the grid boxes [*Ferrier et al.*, 2002].

[27] For the wet scavenging below the precipitating clouds, we use the scavenging coefficient derived by *Seinfeld and Pandis* [1998] for the collection of cloud droplets:

$$E(d_p) = \frac{4}{\mathrm{Re}Sc}\left(1 + 0.4\mathrm{Re}^{1/2}Sc^{1/3} + 0.16\mathrm{Re}^{1/2}Sc^{1/2}\right) + 4\phi\left[\frac{\mu}{\mu_w} + \phi\left(1 + \mathrm{Re}^{1/2}\right)\right] + \left(\frac{St - S^*}{St - S^* + 2/3}\right)^{3/2} \tag{13}$$

where μ and μ_w are the kinematic viscosity of air (1.8×10^{-5} kg m^{-1} s^{-1}) and water (10^{-3} kg m^{-1} s^{-1}), respectively, $\phi = d_p/d_d$ is the ratio of particle to droplet diameter, Re is the Reynolds number for the droplet, S_c is the Schmidt number for the collected particle, and S_t is the Stokes number of the collected particle. Finally, the parameter S^* is given by the following equation:

$$S^* = \frac{1.2 + \ln(1 + \mathrm{Re})/12}{1 + \ln(1 + \mathrm{Re})} \tag{14}$$

4. Sensitivity Tests and Model Evaluation

[28] In order to evaluate the new model performance, a number of sensitivity tests have been designed and executed. The improved SKIRON/Dust system is integrated over the area illustrated in Figures 1–3 that covers northern Africa, the Mediterranean basin, the Middle East, Turkey, and Europe. The model domain is defined in the region with longitude from 24°W to 41°E and latitude from 9°N to 60°N with horizontal grid increment of 0.24°. In the vertical direction, 38 levels are used stretching from the ground to the model top (15800 m). For the majority of the cases, the simulation period extends up to 72 h. The lateral boundary conditions are updated every 3 h. Additional runs have been performed with other resolutions down to 0.03°. For consistency reasons, we discuss here the results with resolution of 0.24°.

4.1. New Soil Characterization

[29] Initially, the improvement of the model performance after the upgrading of the soil characterization was assessed. For this purpose, two model configurations were implemented for simulations with the same input data; one is the "OLD" model version that incorporates all the new features described in the previous section except for the soil characteristics that are described with the aid of the ZÖBLER/FAO and SiB vegetation [*Dorman and Sellers*, 1989] databases and the other is the "NEW" version that resulted after all the proposed modifications, including the STATSGO/FAO soil texture and the USGS vegetation map for the soil characterization. Air temperature observations at 2 m height from the ground were collected from various monitoring stations inside the model domain and compared to the SKIRON outputs. The three hourly observations from about 1300 monitoring stations (about 70% of them in Europe) of the World Meteorological Organization network were used for comparison purposes. For the 3 h mean values during three monthly periods (April 2005, 2006, and 2007), the bias

$$Bias = \frac{1}{N}\sum_{i=1}^{N}(F_i - O_i) = \overline{F} - \overline{O} \tag{15}$$

and the root mean square error (RMSE)

$$RMSE = \sqrt{\frac{1}{N}\sum_{i=1}^{N}(F_i - O_i)^2} \tag{16}$$

resulting from the comparison of all (N) monitoring stations data O_i with the model outputs F_i were calculated. For example, the bias and the RMSE, calculated for the period starting 14 April 2005 at 0000 UTC through 19 April 2005 at 2300 UTC are depicted in Figure 4. The values of the above statistical parameters for all studied periods, together with the correlation coefficient calculated between the simulated and the observed air temperature values are summarized in Table 3. The total number of the observed values (N) used for the comparison with calculations varies from 600 to 1200 for the different measurement hours. The correlation coefficients for both topographic setups range from 0.70 to 0.99. In Figure 4, both the bias and the RMSE appear to increase with forecasting time, while the evolution of the two quantities for the two setups is quite similar. The two statistical parameters acquire higher values during daytime and negative values during the night (between 2300 and 0500 UTC), which implies that the air temperature is overestimated during the day and underestimated in the night. The model has better performance during the minimum and maximum of the diurnal cycle (midnight and midday). The overestimation during the daytime could be possibly attributed to the Geophysical Fluid Dynamics Laboratory (GFDL) radiation scheme, which does not take into consideration the dust effects on incoming solar radiation at the surface and, thus, leads to higher values of surface temperature. This indicates that there is a need for use of a more accurate radiation transfer scheme. As shown in Table 3, the values of bias and RMSE calculated with the new soil description correspond to better forecasts, which are demonstrated through a decrease in bias of 20% and a slight reduction of RMSE (~5%). The correlation coefficient between the simulated and the observed air temperature values does not seem to be altered with the modification of the soil description.

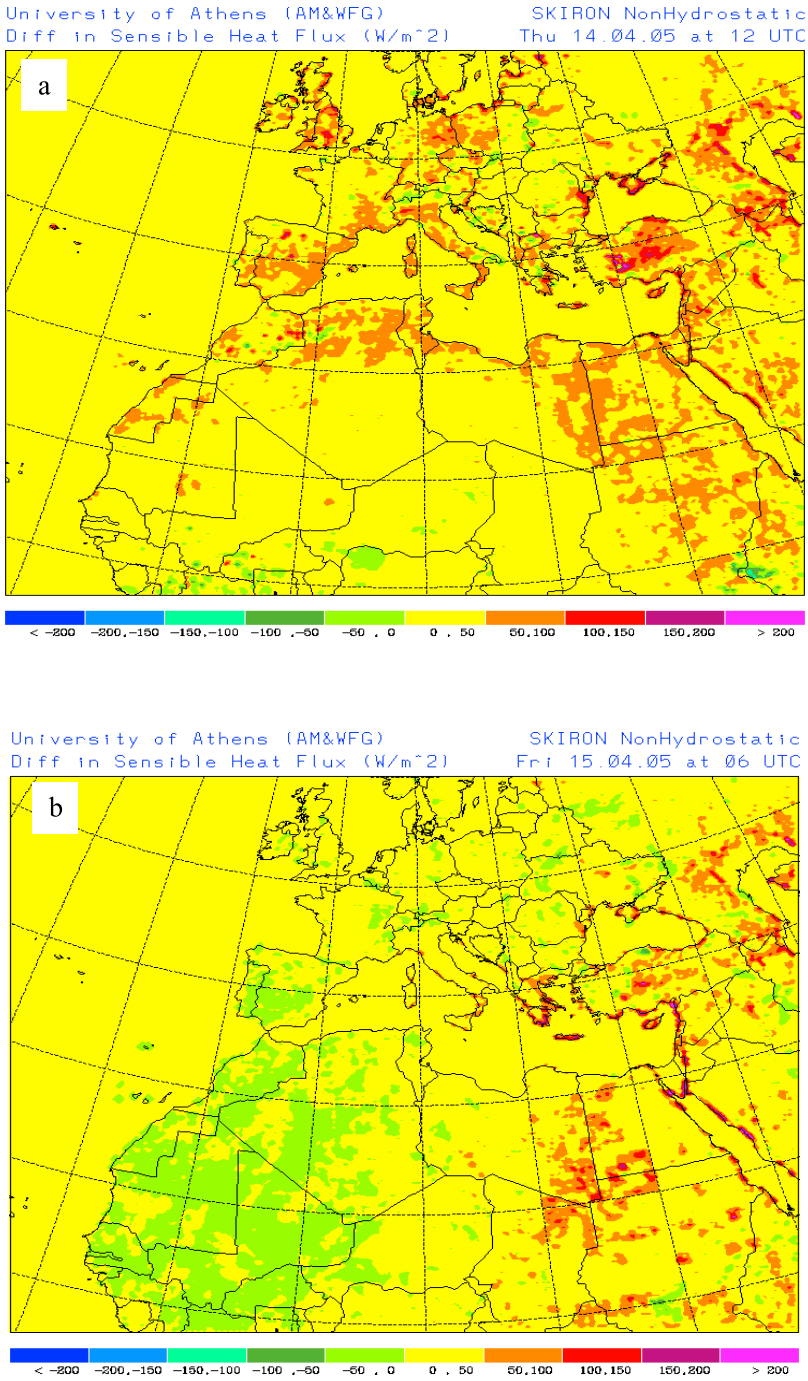

Figure 5. Difference in sensible heat flux by using the grid box orientation and the derived slope and azimuth statistics on each grid box in April 2005 (a) at midday and (b) during morning hours.

However, the high values (089–0.90) throughout all the studied periods reveal a satisfactory model efficiency in the simulations of the near surface temperature fields.

4.2. Terrain Inclination and Radiation Modifications

[30] The impact of utilizing the grid box orientation and the slope and azimuth statistics in each model grid box on the numerical calculations of the atmospheric parameters was examined by performing sensitivity runs with the modeling system. By incorporating the above described (equations (1)–(4)) correction formulas in the radiation algorithm, the received short-wave radiation over slant surfaces can now be determined with a greater spatial resolution. The deviations in the radiation fluxes are expected to have a noticeable impact on the atmospheric parameters, such as air temperature, wind fields, and turbulence. The derived simulated values after including the statistics are compared to the model outputs of a run initiated on 14 April 2005 at 0000 UTC. In the former model configuration, all the new features described in the previous section are

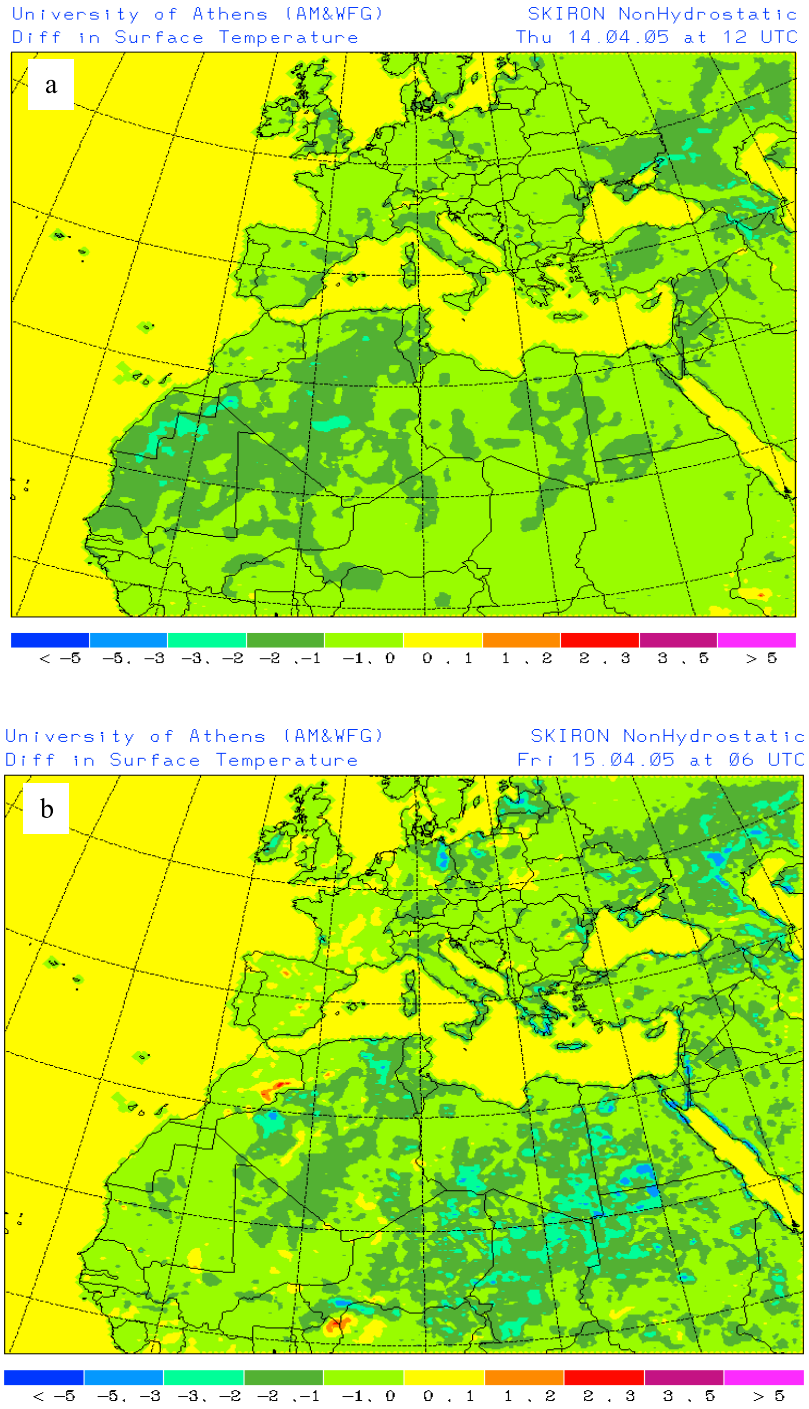

Figure 6. Difference in air temperature at 2 m height by using the grid box orientation and the derived slope and azimuth statistics on each grid box in April 2005 (a) at midday and (b) during morning hours.

considered including the statistical corrections related to the terrain slopes (case A), while the comparative model setup incorporates the new features except the slope statistics (case B). The difference in the sensible heat flux and the air temperature close to the ground surface between the model runs by using the original grid box orientation or the derived slope and azimuth statistics on each grid box for determining the received short-wave radiation at the ground surface (case B – case A) are depicted in Figures 5 and 6, respectively, for midday and morning hours. Deviations in the derived parameters can be noticed with the correction of terrain slopes and azimuths in different sites of the domain for different hours of the day. In particular, the discrepancies are more evident in the areas facing the east during the morning hours and the areas facing the west at noon. In both cases (morning and noon), the deviations are detected mostly upon areas of rough terrain that also release considerable amounts of thermal radiation

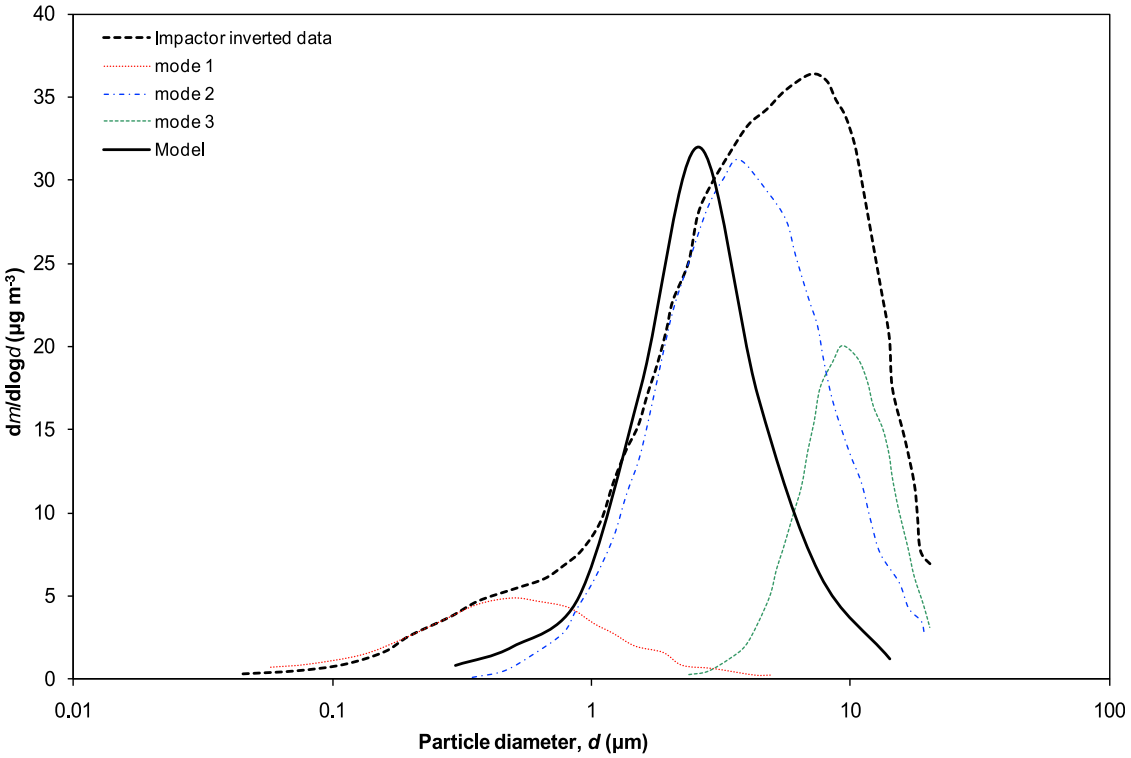

Figure 7. Mass size distributions of dust particles during the spring dust episode on 5 March 2005 in Crete, Greece (black dashed line, impactor inverted data; red, blue, and green lines, differential modes of the distribution; solid black line, model outputs).

(e.g., arid areas north of the equator, Morocco, and coastal sites of Red Sea). The differences in the sensible heat flux at the ground surface could reach up to 200 W m^{-2}, while the respective deviations in the outgoing long-wave radiation are calculated at about 20–30 W m^{-2} and are greater over areas of rough terrain. In the case of the air temperature values, the variations between the two different approaches are found to reach 3°C to 4°C in the warmer areas of the domain and upon surfaces with noticeable inclination (central Europe, Balkan Peninsula, eastern Black sea region). It should be noted though that the results presented here cover a typical spring case; the respective differences noticed in the winter and autumn periods are lower than expected because of the smaller radiation amounts received by the ground surface. In general, the detailed consideration of slopes and azimuths at higher resolution has as a result the more explicit calculation of the incoming solar radiation and therefore the energy partitioning at the surface. Moreover, by considering more detailed terrain sloping in the model grid box, a better positioning of the convergence zones at the mountainous regions can be achieved.

4.3. Dust Particle Size Distribution

[31] For the evaluation of the dust particle size distribution, as determined by the SKIRON modeling system, our model results were compared against experimental data of mass distribution in the island of Crete, Greece, presented by *Gerasopoulos et al.* [2007]. The latter authors studied the seasonal mass size distributions at a coastal site situated 70 km to the east/northeast of Heraklion (Finokalia); they applied collection efficiency curves of the impactor on the raw data and they fitted lognormal distributions in order to separate the various modes of each distribution. The continuous curve of the impactor inverted data collected at 4–6 March 2005 and the three modes of the distribution are depicted in Figure 7, together with the model results for the dust episode of the 5 March 2005. The particle mass size distribution, as simulated by SKIRON, is closer with the "coarse 2" mode (blue line), which is derived from the analysis of the experimental data that is mainly attributed to African dust transport and describes adequately the left finer part of the distribution mode. However, the dust concentration curve derived from the model calculations presents a small but observable shift toward lower diameter values compared to the second mode of the experimentally derived distribution curve and it seems to underestimate noticeably the right coarser part of the mode and the "extra coarse" mode (green line) that is also related to dust, as the authors claim. Thus, it is evident that the selection of the long-range transport mode of *Schulz et al.* [1998] adopted in the new SKIRON version cannot provide effective calculations of the particle size distribution during sand storms, where larger particles (average diameter greater than 16 μm according to *Ahmed et al.* [1987]) are suspended. Moreover, the dust module of the modeling system considers a constant long-range transport mode at any distance from the dust source areas. The consideration of a variant particle size distribution as a function of the distance that the dust particles have traversed would probably lead to more accurate calculations and better agreement with the experimental measurements. However,

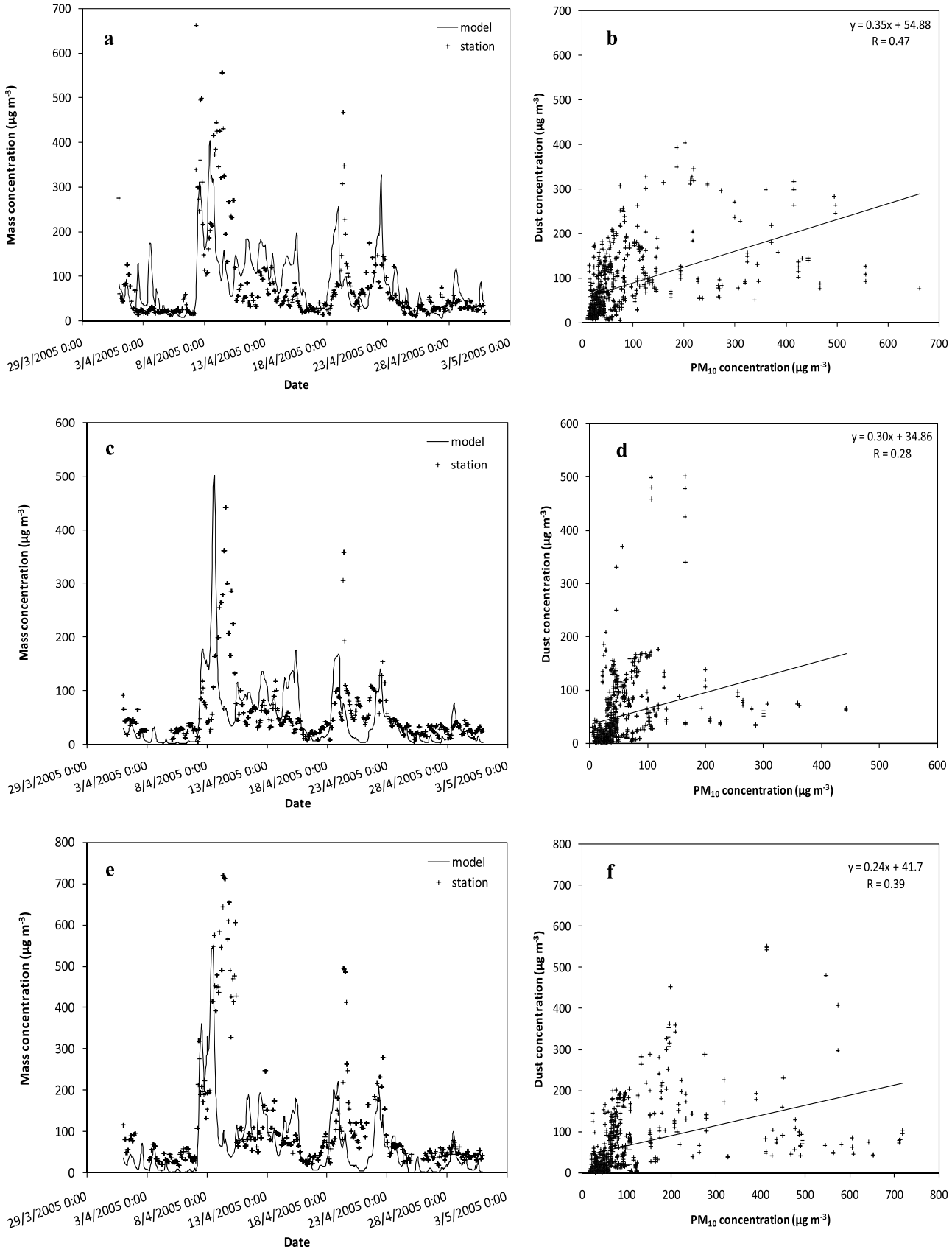

Figure 8. (a, c, e) Time series of the mass concentration and (b, d, f) scatter plots between modeled dust and observed PM_{10} concentration values for April 2005 at Israel monitoring stations: Beersheba (Figures 8a and 8b), Afula (Figures 8c and 8d), and Modiin (Figures 8e and 8f).

Table 4. AERONET Stations, Their Geographical Coordinates, and the Altitude

AERONET Station	Latitude	Longitude	Altitude (m)
Lampedusa	N35°31′01″	E12°37′55″	45
Crete	N35°19′58″	E25°16′55″	20
Athens	N37°59′16″	E23°46′30″	130
Blida	N36°30′28″	E02°52′51″	230
Tamanrasset	N22°47′24″	E05°31′48″	1377

the use of the current distribution mode is adequate for long-range transported desert dust but more particle size bins are needed toward the large particles to consider the sand storm-produced particles near the sources.

4.4. Dust Concentration and AOD Evaluation

[32] The performance of the new model version for the calculation of dust concentrations has been evaluated with the aid of measurement data. First, model estimates of near-ground dust concentrations have been compared with PM_{10} observations available to us from three monitoring stations of the Israeli Ministry of the Environment (Beersheba, 31°15′N, 34°47′E; Afula, 32°32′N, 35°23′E; and Modiin, 31°54′N, 35°00′E) and for the period covering April 2005. The time series of mass concentration as well as the scatter plots between predicted dust concentrations and measured PM_{10} concentrations are illustrated in Figure 8. The time series plots exhibit considerable temporal coincidence of the maxima and minima for the compared data sets during the whole month period and in all three selected areas. Specifically, during the dust event occurred on 22 April, the particle mass concentration reached up to 280 μg m^{-3} in Modiin, while the SKIRON model captured satisfactorily the observed values especially in Afula station. A stronger dust episode in the period between 8 and 10 April can be detected in the time series of all monitoring sites. The model predicted

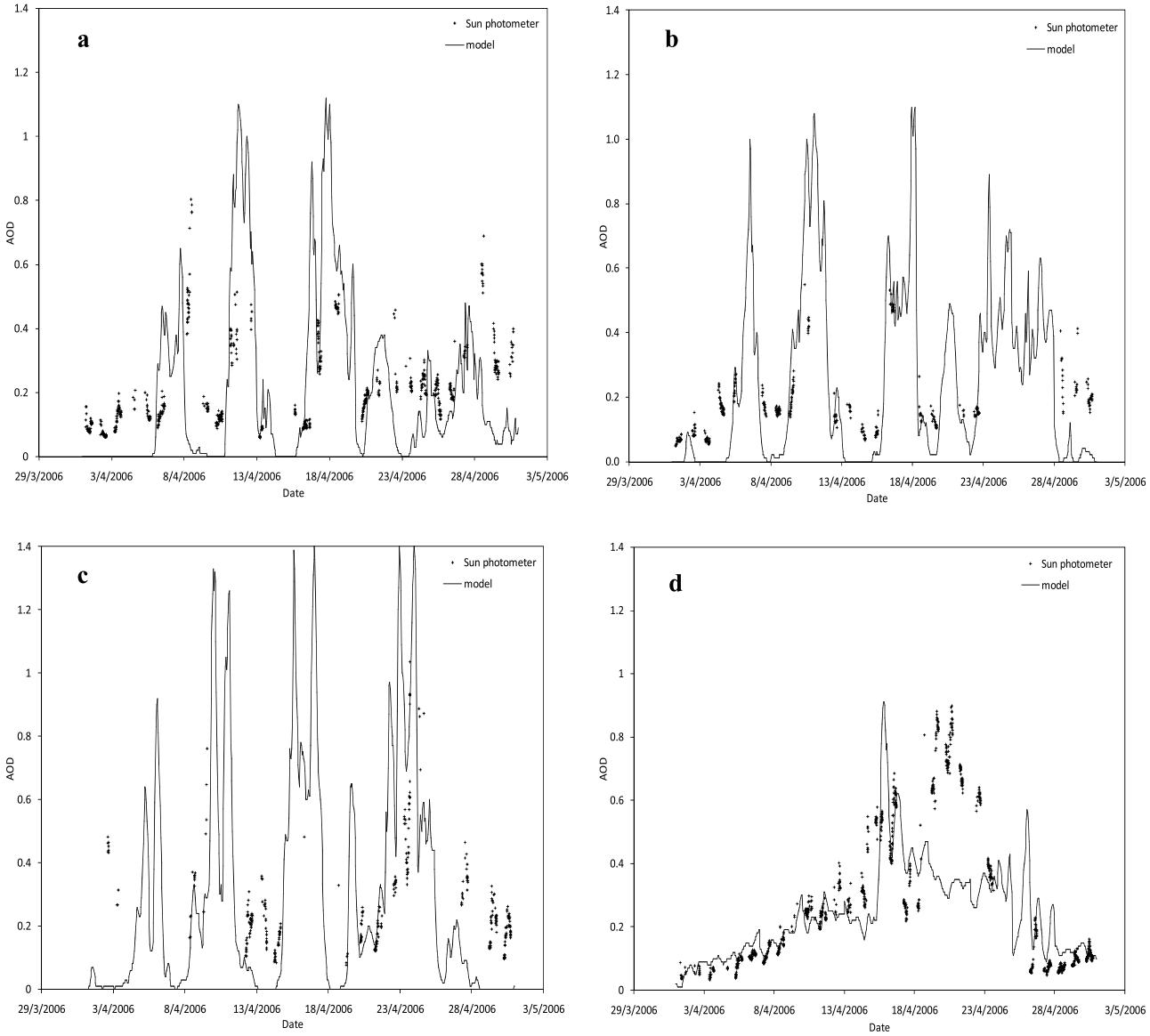

Figure 9. Observed and modeled time series of the interpolated AOD at 532 nm for April 2006 at (a) Crete, (b) Lampedusa, (c) Blida, and (d) Tamanrasset.

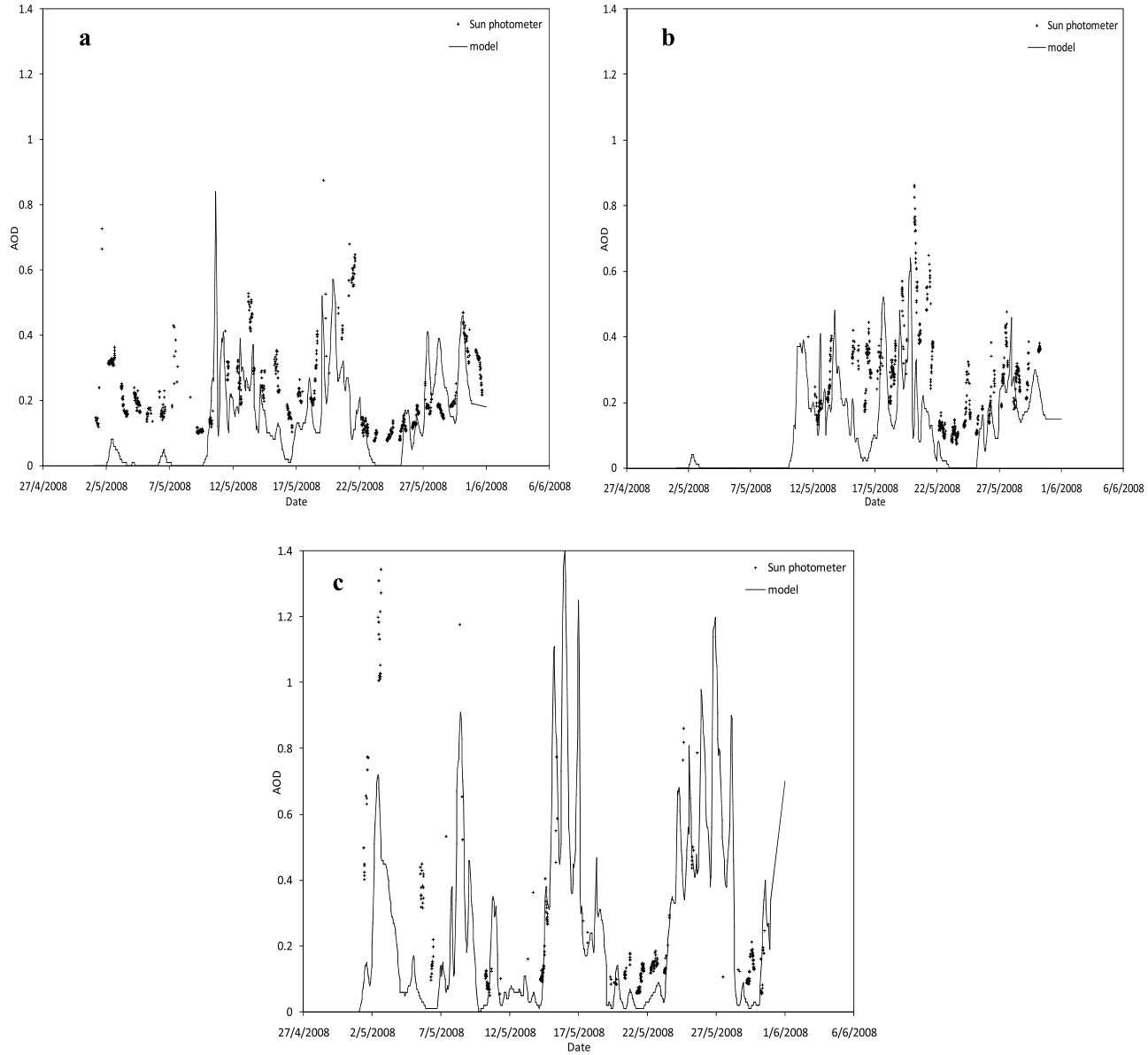

Figure 10. Observed and modeled time series of the interpolated AOD at 532 nm for May 2008 at (a) Crete, (b) Athens, and (c) Blida.

the particle mass increase approximately 12 h earlier, but the simulated intensity of the episode expressed in terms of mass concentration was very close to the observed one. These time shifts lead to rather poor estimates of the correlation coefficients, with a lower value in Afula (0.3) and a higher value in Beersheba (0.5). In the scatter diagrams, both small and large concentrations are included, which also may lead to this poor correlation. It should be noted though that the monitored PM_{10} concentrations include the mass suspended particles from other sources besides desert dust (e.g., anthropogenic sources of PMs). However, the slope of the trend line (0.35 at Beersheba, 0.30 at Afula, and 0.24 at Moddin), which is indicative of the fraction of mineral dust in PM_{10} concentration, reveals a significant contribution of dust to aerosol for the Israeli stations during the whole month. The above slope values would be even greater if the model calculated the mass concentration of the larger suspended dust particles more accurately since Israel is located near the source areas and therefore particles greater than PM_{10} are monitored.

[33] Model run AOD calculations at 532 nm were compared with measured values originating from Sun photometer data of the AERONET network [*Holben et al.*, 1998] (level 1.5) over the periods of April 2006 and May 2008. During each spring period, at least two dust events occurred in a number of selected monitoring stations (Lampedusa, Crete, Athens, Blida, and Tamanrasset), the characteristics (coordinates and altitude) of which are shown in Table 4. The selection of the specific sites was based on the occurrence of dust load maxima during the studied periods and the representativeness of the dust affected Mediterranean areas. The level 2.0 quality-controlled data of the network were not used in the present analysis since they were not available for all selected sites and periods (e.g., Crete for May 2008) and they

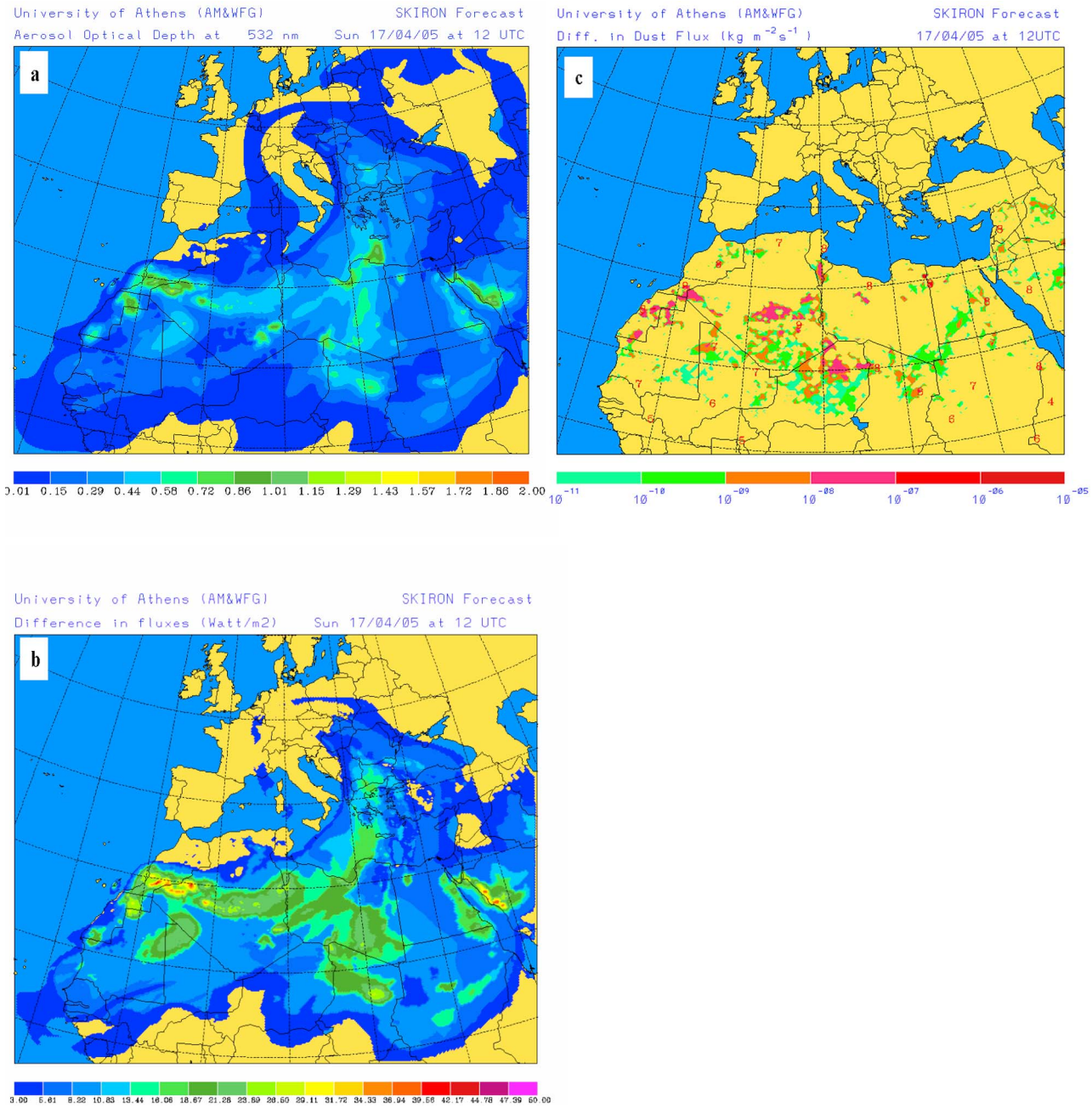

Figure 11. (a) Aerosol optical depth at 532 nm, (b) difference in incoming solar radiation due to the extinction by dessert dust particles, and (c) difference in dust flux due to the reduction of the incoming solar radiation for 17 April 2005.

included large gaps during dust episodes. Following *Pérez et al.* [2006], the AOD values at a specific wavelength λ were derived via the particle physical characteristics:

$$AOD(\lambda) = \sum_{i=1}^{8} \frac{3}{4\rho_{pi} r_i} M_i Q_e(\lambda)_i \tag{17}$$

where M_i is the particle mass load of the i^{th} size bin and $Q_e(\lambda)_i$ is the extinction coefficient factor, as calculated from the Mie scattering theory. In order to estimate the AOD from the data sets provided by the monitoring stations at the fixed wavelength of 532 nm, we first calculated the Ångström exponent that is derived from the ratio between the AOD at two adjacent wavelengths (λ_1 and λ_2), through the following equation:

$$a = \frac{\ln(AOD_{\lambda_1}/AOD_{\lambda_2})}{\ln(\lambda_2/\lambda_1)} \tag{18}$$

Then, the optical depth at 532 nm can be easily calculated through the interpolation formula described in *Iqbal* [1983]. The AOD values that correspond to 440 and 870 nm, provided by the AERONET network, were used for the calculation of the AOD at 532 nm for each monitoring

Table 5. Trend Lines and Correlation Coefficients Between Modeled and Measured Incoming Solar Flux at Crete and Sede Boker during April 2005, 2006, and 2007[a]

Month and Year	Crete	Sede Boker
	No Dust Effect	
Apr 2005	$y = 1.047x + 64.94$, $R^2 = 0.838$	$y = 1.055x + 72.93$, $R^2 = 0.782$
Apr 2006	$y = 1.060x + 68.09$, $R^2 = 0.818$	$y = 1.070x + 63.11$, $R^2 = 0.825$
Apr 2007	$y = 1.056x + 54.36$, $R^2 = 0.865$	$y = 1.019x + 85.01$, $R^2 = 0.723$
	Dust Effect	
Apr 2005	$y = 1.034x + 64.23$, $R^2 = 0.835$	$y = 1.042x + 71.59$, $R^2 = 0.783$
Apr 2006	$y = 1.050x + 66.73$, $R^2 = 0.821$	$y = 1.056x + 62.52$, $R^2 = 0.822$
Apr 2007	$y = 1.055x + 54.36$, $R^2 = 0.863$	$y = 1.006x + 84.46$, $R^2 = 0.721$

[a]Trend lines and correlation coefficients take into account and neglecting dust effect.

station. Figures 9 and 10 show the time series of the AOD at 532 nm for the various monitoring sites and during the two aforementioned periods. Pronounced gaps in the data series are observed, especially for the station of Lampedusa and to a lesser extent in Blida. The measured AOD reaches the value 0.8 over Greece (i.e., Crete, Athens) and in Lampedusa and exceeds the value 1 at the dust source area of Blida. In general, the model outputs follow the trend of the observational values in all selected areas and for some specific dust events; the simulated values are very close to the monitored ones. For example, the model captured quite well the dust episode that occurred in Greece in the end of May 2008. On the other hand, the model underestimates largely the event that occurred in the beginning of May 2008 in the station of Blida. This underestimation could be attributed to the selected particle size distribution (long-range transport mode) in SKIRON model that describes satisfactorily the finest mode of the dust-transported aerosol, but neglects the major fraction of the coarser dust particles suspended mainly over or close to dust source areas. In other cases, the model captured correctly the onset of a dust episode, such as the one occurred in early April 2006 in Tamanrasset, but the effective simulation of the episode intensity, in terms of AOD values, cannot be estimated because of many missing values in the dataset of the monitoring station.

4.5. Impact of Dust Aerosol on Radiation

[34] A significant advance of the developed modeling system is the feasibility of estimating the effect of dust particles on atmospheric parameters. In particular, the impact of the presence of dust particles in the atmosphere on the radiative transfer is taken into consideration. It is known that dust particles scatter incoming solar radiation, thus the radiant energy reaching the ground surface is expected to be reduced. The model takes into account this process through the determination of AOD values for eight size bins (see equation (17)). Then the decrease of the incoming SW solar radiation is calculated by using lookup tables for the different AOD values [*Kaufman et al.*, 2002]. Figure 11a depicts the AOD calculated by the atmospheric/dust transport modeling system at 532 nm and for 17 April 2005. Figure 11b illustrates the reduction in the incoming solar radiation due to the extinction by desert dust particles. As expected, the radiation flux decrease is more

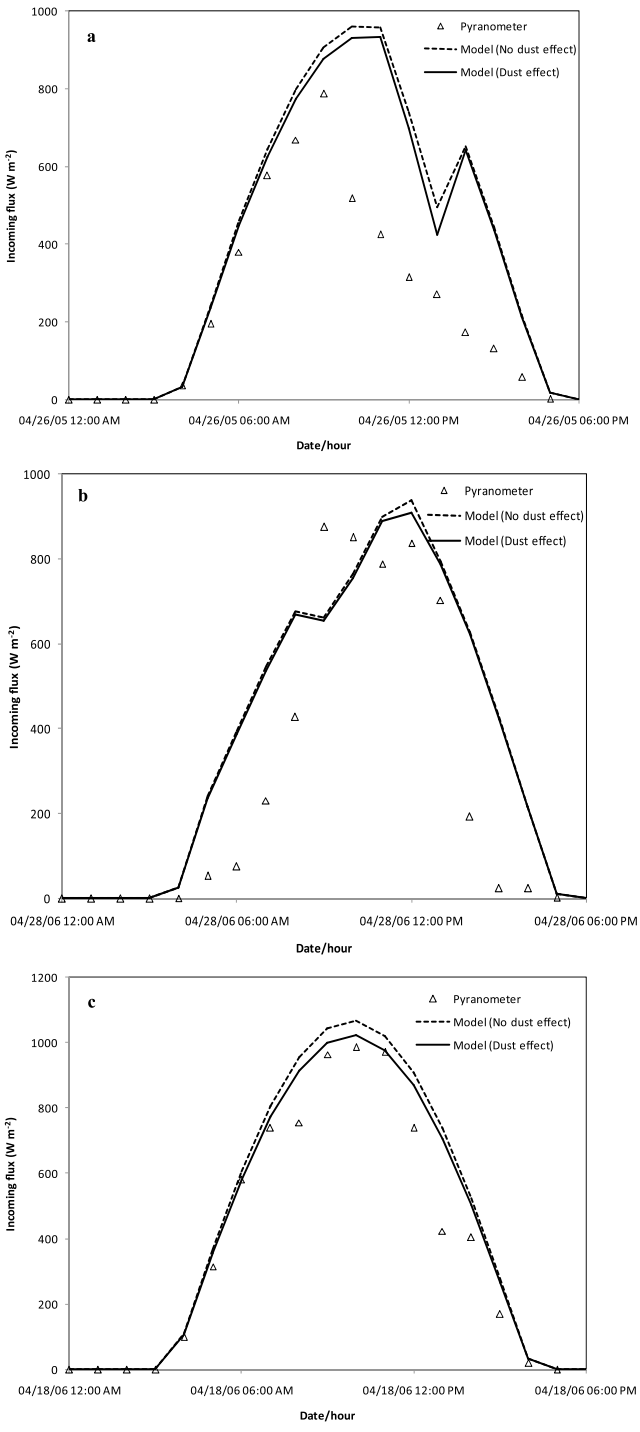

Figure 12. Time series of modeled (taking into account and neglecting dust effect) and measured incoming solar flux for specific dust events on (a) 26 April 2005 and (b) 28 April 2006 at Crete and (c) 18 April 2006 at Sede Boker.

pronounced over areas with increased dust concentration, reaching 40 W m^{-2} in northern Africa and the Middle East during the specific episode. For other cases, the decrease was even higher in some locations in the Mediterranean. The latter decrease in value is in agreement with the respective ones estimated by *di Sarra et al.* [2008, and references therein] for the radiative forcing due to desert dust particles. It should be noted though that the radiative forcing values were found to exhibit a significant spatial and temporal fluctuation. A noticeable outcome of the radiation reduction is the suppression of the dust productivity. Thus, in the dust source areas of the model domain, the incoming solar flux appears to decrease, which in return leads to reduction of the dust flux and decrease of the dust aerosol production, as shown in Figure 11c. In order to evaluate the calculation of the radiative forcing, the radiation flux measurements obtained during dust events in the spring periods of April 2005, 2006, and 2007 at two sites of the AERONET network, namely, (Crete TEI (35°18′N, 25°06′E) and Sede Boker (30°51′N, 34°47′E) were utilized. The trend lines and the correlation coefficients between modeled and measured solar flux values for the three monthly periods are presented in Table 5. The modeled flux values have been determined for two different configurations: for taking into consideration the dust effect on SW radiation and for neglecting the radiative dust effects. In general, the SKIRON model simulates the SW radiation that reaches the ground surface satisfactorily. The slope of the trend lines are very close to unity and the correlation coefficients R^2 fluctuate between 0.72 and 0.87. However, by isolating the periods with enhanced aerosol concentration, as obtained by the increased AOD measured values at the AERONET sites, remarkable improvements in the determination of the maximum incoming SW flux may be noticed by including the aerosol shading effect in SKIRON calculations (Figure 12). In particular, on 26 April 2005, the model overestimation of the incoming flux at Crete was decreased by 16% by taking into account the dust shading effect (Figure 12a) and on 28 April 2006 a reduction of the overestimation by 28% was achieved (Figure 12b). For the Sede Boker site, the incorporation of the dust effect on SW radiation in SKIRON model led to better simulations of the radiation reduction due to the presence of aerosol particles by up to 57% on 18 April 2006 (Figure 12c). The GFDL radiative transfer scheme in SKIRON model is known for overestimating the incoming solar radiation at the surface because it does not include aerosol effects. With the suggested corrections due to the presence of dust, this overestimation is becoming less. A more explicit study on the radiation effects of aerosol particles, considering the long-wave radiation transfer impacts, is included in the authors' future plans.

5. Discussion and Conclusions

[35] On the basis of the present status of the modeling tools that simulate mineral dust processes in the atmosphere and effects on climate, a combined effort was devoted to the incorporation of certain advancements and new features in SKIRON/Dust forecasting system. The inclusion of more accurate schemes led to better simulations of the atmospheric fields and the mineral dust properties.

[36] The comparison of the model outputs with available observations from an extended and dense monitoring network showed that the atmospheric model predictions are improved significantly by the introduction of the new soil characterization schemes. However, the model overestimation of the air temperature values is attributed mainly to the existing radiative transfer scheme. This implies the need for better radiation calculations; the examination of radiation scheme upgrading is under consideration for future work. The radiation balance appears to be affected by the presence of steep slopes on the ground terrain and the suspension of dust particles in the atmosphere. The differences in the calculated sensible heat flux, by considering slope statistics, could reach up to 200 W m^{-2} in areas where high amounts of thermal radiation are released and air temperature deviations were about 3°C to 4°C. Differences of 20–30 W m^{-2} were also found in the calculated values of the outgoing long-wave radiation after the corrections performed on the terrain slopes and azimuths. The radiation differences were mainly accumulated in areas with highly rough terrain.

[37] Significant improvements were incorporated in the description and physical processes of dust aerosol. By increasing the size bins of the dust particle mass distribution, the magnitude of the suspended particles can be calculated accurately. The lognormal distribution that has been attributed to desert dust concentration through chemical analysis has been reproduced satisfactorily by the model for the smaller particle bins. A more accurate representation of the transported dust aerosol distribution could be possibly achieved with the utilization of a variant long-range transported mode as a function of the distance from the dust sources. The new dust production and deposition schemes provide the capability of an efficient determination of particle optical properties. The incorporation of the dust production and deposition mechanisms led to adequate calculations of the dust concentration near the ground level and the aerosol optical depth in various sites of the Mediterranean region. The optical depth values allowed the determination of the short-wave radiation decrease induced by the presence of dust particles and reduced the model overestimation in the incoming SW flux during dust events by up to 57%.

[38] **Acknowledgment.** This work has been supported by the European Union 6th Framework Program CIRCE IP, contract 036961.

References

Ackerley, D., E. J. Highwood, M. A. J. Harrison, C. L. McConnell, M. M. Joshi, D. N. Walter, S. F. Milton, G. Greed, and M. E. Brooks (2009), The development of a new dust uplift scheme in the Met Office Unified Model, *Meteorol. Appl.*, *16*, 445–460, doi:10.1002/met.141.

Ahmed, A. S., A. A. Ali, and M. A. Alhaider (1987), Measurement of atmospheric particle size distribution during sand/dust storm in Riyadh, Saudi Arabia, *Atmos. Environ.*, *21*(12), 2723–2725.

Alfaro, S. C., and L. Gomes (2001), Modeling mineral aerosol production by wind erosion: Emission intensities and aerosol size distributions in source areas, *J. Geophys. Res.*, *106*(D16), 18,075–18,084.

Anderson, J., E. Hardy, J. Roach, and R. Witmer (1976), A land use and land cover classification system for use with remote sensing data, *U.S. Geol. Prof. Pap. 964*, U.S. Gov. Print. Off., Washington, D. C.

Bagnold, R. A. (2005), *The Physics of Blown Sand and Desert*, Dover, Mineola, N. Y.

Charlson, R. J., J. Langner, H. Rodhe, C. B. Leovy, and S. G. Warren (1991), Perturbation of the Northern Hemisphere radiative balance by backscattering from anthropogenic sulfate aerosols, *Tellus*, *43*(4), 152–163.

D'Almeida, G. A. (1987), On the variability of desert aerosol radiative characteristics, *J. Geophys. Res.*, *92*(D3), 3017–3026.

di Sarra, A., G. Pace, D. Meloni, L. De Silvestri, S. Piacentino, and F. Monteleone (2008), Surface shortwave radiative forcing of different aerosol types in the central Mediterranean, *Geophys. Res. Lett.*, *35*, L02714, doi:10.1029/2007GL032395.

Dorman, J. L., and P. J. Sellers (1989), A global climatology of albedo, roughness length and stomatal resistance for atmospheric general circulation models as represented by the Simple Biosphere Model (SiB), *J. Appl. Meteorol.*, *28*(9), 833–855.

ENVIRON (Ed.) (2006), *User's Guide to the Comprehensive Air Quality Model with Extensions (CAMx)*, version 4.31, Novato, Calif.

Fécan, F., B. Marticorena, and G. Bergametti (1999), Parameterization of the increase of the aeolian erosion threshold wind friction velocity due to soil moisture for arid and semi-arid areas, *Ann. Geophys.*, *17*, 149–157.

Ferrier, B. S., Y. Jin, Y. Lin, T. Black, E. Rogers, and G. DiMego (2002), Implementation of a new grid-scale cloud and precipitation scheme in the NCEP Eta model, paper presented at 15th Conference on Numerical Weather Prediction, Am. Meteorol. Soc., San Antonio, Tex.

Georgi, F. (1986), A particle dry-deposition parameterization scheme for in tracer transport models, *J. Geophys. Res.*, *91*, 9794–9806.

Gerasopoulos, E., E. Koulouri, N. Kalivitis, G. Kouvarakis, S. Saarikoski, T. Mäkelä, R. Hillamo, and N. Mihalopoulos (2007), Size-segregated mass distributions of aerosols over Eastern Mediterranean: Seasonal variability and comparison with AERONET columnar size-distributions, *Atmos. Chem. Phys.*, *7*(10), 2551–2561.

Gillette, D. A. (1977), Fine particle emissions due to wind erosion, *Trans. ASAE*, *20*, 891–897.

Ginoux, P., M. Chin, I. Tegen, J. M. Prospero, B. Holben, O. Dubovik, and S. J. Lin (2001), Sources and distributions of dust aerosols simulated with the GOCART model, *J. Geophys. Res.*, *106*, 20,255–20,273.

Gong, S. L., X. Y. Zhang, T. L. Zhao, I. G. McKendry, D. A. Jaffe, and N. M. Lu (2003), Characterization of soil dust aerosol in China and its transport and distribution during 2001 ACE-Asia: 2. Model simulation and validation, *J. Geophys. Res.*, *108*(D9), 4262, doi:10.1029/2002JD002633.

Grossman-Clarke, S., J. A. Zehnder, W. L. Stefanov, Y. Liu, and M. A. Zoldak (2005), Urban modifications in a mesoscale meteorological model and the effects on near-surface variables in an arid metropolitan region, *J. Appl. Meteorol.*, *44*, 1281–1297.

Heinold, B., I. Tegen, K. Schepanski, and O. Hellmuth (2008), Dust radiative feedback on Saharan boundary layer dynamics and dust mobilization, *Geophys. Res. Lett.*, *35*, L20817, doi:10.1029/2008GL035319.

Hodur, R. M. (1997), The Naval Research Laboratory's Coupled Ocean/Atmosphere Mesoscale Prediction System (COAMPS), *Mon. Weather Rev.*, *125*(7), 1414–1430.

Holben, B. N., T. F. Eck, I. Slutsker, D. Tanre, J. P. Buis, A. Setzer, E. Vermote, J. A. Reagan, Y. J. Kaufman, T. Nakajima, et al. (1998), AERONET—A federated instrument network and data archive for aerosol characterization, *Remote Sens. Environ.*, *66*, 1–16.

Iqbal, M. (1983), *An Introduction to Solar Radiation*, Academic, Toronto, Ont. Canada.

Iversen, J. D., J. B. Pollack, R. Greeley, and B. R. White (1976), Saltation threshold on Mars: The effect on interparticle force, surface roughness, and low atmospheric density, *Icarus*, *29*, 381–393.

Janjic, Z. I. (1984), Nonlinear advection schemes and energy cascade on semi-staggered grids, *Mon. Weather Rev.*, *112*, 1234–1245.

Kallos, G., S. Nickovic, D. Jovic, O. Kakaliagou, A. Papadopoulos, N. Misirlis, L. Boukas, and N. Mimikou (1997), The ETA model operational forecasting system and its parallel implementation, paper presented at 1st Workshop on Large-Scale Scientific Computations, Varna, Bulgaria, 7–11 June.

Kallos, G., A. Papadopoulos, P. Katsafados, and S. Nickovic (2006), Transatlantic Saharan dust transport: Model simulation and results, *J. Geophys. Res.*, *111*, D09204, doi:10.1029/2005JD006207.

Katsafados, P., A. Papadopoulos, and G. Kallos (2005), Regional atmospheric response to tropical Pacific SST perturbations, *Geophys. Res. Lett.*, *32*, L04806, doi:10.1029/2004GL021828.

Kaufman, Y. J., D. Tanré, B. N. Holben, S. Mattoo, L. A. Remer, T. F. Eck, J. Vaughan, and B. Chatenet (2002), Aeronet radiative impact on spectral solar flux at the surface, derived from principal-plane sky measurements, *J. Atmos. Sci.*, *59*(3), 635–646.

Kelly, J. T., C. C. Chuang, and A. S. Wexler. (2007), Influence of dust composition on cloud droplet formation, *Atmos. Environ.*, *41*(14), 2904–2916.

Kumar, N., F. W. Lurmann, A. S. Wexler, S. Pandis, and J. H. Seinfeld (1996), Development and application of a three-dimensional aerosol model, paper presented at Speciality Conference on Computing in Environmental Resource Management, Air and Waste Manage. Assoc., Durham, N. C.

Levin, Z., A. Teller, E. Ganor, and Y. Yin (2005), On the interactions of mineral dust, sea-salt particles, and clouds: A measurement and modeling study from the Mediterranean Israeli Dust Experiment campaign, *J. Geophys. Res.*, *110*, D20202, doi:10.1029/2005JD005810.

Liu, M., D. L. Westphal, S. Wang, A. Shimizu, N. Sugimoto, J. Zhou, and Y. Chen (2003), A high-resolution numerical study of the Asian dust storms of April 2001, *J. Geophys. Res.*, *108*(D23), 8653, doi:10.1029/2002JD003178.

Marticorena, B., and G. Bergametti (1995), Modeling the atmospheric dust cycle: 1. Design of a soil-derived dust emission scheme, *J. Geophys. Res.*, *100*, 16,415–16,430.

Marticorena, B., G. Bergametti, B. Aumont, Y Callot, C. N'Doumé, and M. Legrand (1997), Modeling the atmospheric dust cycle: 2. Simulation of Saharan dust sources, *J. Geophys. Res.*, *102*, 4387–4404.

Mesinger, F. (1984), A blocking technique for representation of mountains in atmospheric models, *Riv. Meteorol. Aeronaut.*, *44*, 195–202.

Miller, D. A., and R. A. White (1998), A conterminous United States multilayer soil characteristics data set for regional climate and hydrology modeling, http://EarthInteractions.org, *Earth Interactions*, *2*, 1–26.

Nickovic, S., G. Kallos, A. Papadopoulos, and O. Kakaliagou (2001), A model for prediction of desert dust cycle in the atmosphere, *J. Geophys. Res.*, *106*(D16), 18,113–18,129.

Papadopoulos, A. (2001), A limited area model with enhanced capabilities for handling initial and boundary conditions (in Greek), Ph.D. thesis, Univ. of Athens, Athens.

Pérez, C., S. Nickovic, J. M. Baldasano, M. Sicard, F. Rocadenbosch, and V. E. Cachorro (2006), A long Saharan dust event over the western Mediterranean: Lidar, Sun photometer observations, and regional dust modeling, *J. Geophys. Res.*, *111*, D15214, doi:10.1029/2005JD006579.

Pielke, R. A. (2002), *Mesoscale Meteorological Modelling*, 676 pp., Academic, San Diego, Calif.

Reynolds, J. F., R. A. Virginia, P. R. Kemp, A. G. de Soyza, and D. C. Tremmel (1999), Impact of drought on desert shrubs: Effects of seasonality and degree of resource island development, *Ecol. Monogr.*, *69*, 69–106.

Schulz, M., Y. J. Balkanski, W. Quelle, and F. Dulac (1998), Role of aerosol size distribution and source location in a three-dimensional simulation of a Saharan dust episode tested against satellite-derived optical thickness, *J. Geophys. Res.*, *103*(3339), 10,579–10,592.

Segal, M., J. R. Garatt, G. Kallos, and R. A. Pielke (1989), The impact of wet soil and canopy temperatures on daytime boundary-layer growth, *J. Atmos. Sci.*, *46*(24), 3673–3684.

Seinfeld, J. H., and S. N. Pandis (1998), *Atmospheric Chemistry and Physics: From Air Pollution to Climate Change*, 1326 pp., John Wiley, New York.

Song, C. H., and G. R. Carmichael (2001), A three-dimensional modeling investigation of the evolution processes of dust and sea-salt particles in east Asia, *J. Geophys. Res.*, *106*(D16), 18,131–18,154.

Steyn, D. G. (1976), Computation of azimuths, slope angles and surface normals over a given topography, *S. Afr. J. Geogr.*, *58*, 130–133.

Uno, I., et al. (2003), Regional chemical weather forecasting system CFORS: Model descriptions and analysis of surface observations at Japanese island stations during the ACE-Asia experiment, *J. Geophys. Res.*, *108*(D23), 8668, doi:10.1029/2002JD002845.

Uno, I., et al. (2006), Dust model intercomparison (DMIP) study over Asia: Overview, *J. Geophys. Res.*, *111*, D12213, doi:10.1029/2005JD006575.

White, B. R. (1979), Soil transport by winds on Mars, *J. Geophys. Res.*, *84*, 4643–4651.

Yu, S., C. S. Zender, and V. K. Saxena (2001), Direct radiative forcing and atmospheric absorption by boundary layer aerosols in the southeastern US: Model estimates on the basis of new observations, *Atmos. Environ.*, *35*, 3967–3977.

Zakey, A. S., F. Solmon, and F. Giorgi (2006), Implementation and testing of a desert dust module in a regional climate model, *Atmos. Chem. Phys.*, *6*(12), 4687–4704.

Zender, C. S., H. Bian, and D. Newman (2003), Mineral Dust Entrainment and Deposition (DEAD) model: Description and 1990s dust climatology, *J. Geophys. Res.*, *108*(D14), 4416, doi:10.1029/2002JD002775.

Zhou, C. H., S. L. Gong, X. Y. Zhang, Y. Q. Wang, T. Niu, H. L. Liu, T. L. Zhao, Y. Q. Yang, and Q. Hou (2008), Development and evaluation of an operational SDS forecasting system for East Asia: CUACE/Dust, *Atmos. Chem. Phys.*, *8*(4), 787–798.

Zöbler, L. (1986), A world soil file for global climate modelling, *Tech. Memo. 87802*, NASA Goddard Inst. for Space Stud., New York.

G. Kallos, P. Louka, C. Mitsakou, C. Spyrou, and G. Vlastou, School of Physics, University of Athens, Bldg. Phys-5, GR-15784 Athens, Greece. (kallos@mg.uoa.gr)